



HAL
open science

Modeling spectral lags in active galactic nucleus flares in the context of Lorentz invariance violation searches

C. Perennes, H. Sol, J. Bolmont

► To cite this version:

C. Perennes, H. Sol, J. Bolmont. Modeling spectral lags in active galactic nucleus flares in the context of Lorentz invariance violation searches. 2019. hal-02409304v1

HAL Id: hal-02409304

<https://hal.science/hal-02409304v1>

Preprint submitted on 13 Dec 2019 (v1), last revised 7 Jan 2021 (v2)

HAL is a multi-disciplinary open access archive for the deposit and dissemination of scientific research documents, whether they are published or not. The documents may come from teaching and research institutions in France or abroad, or from public or private research centers.

L'archive ouverte pluridisciplinaire **HAL**, est destinée au dépôt et à la diffusion de documents scientifiques de niveau recherche, publiés ou non, émanant des établissements d'enseignement et de recherche français ou étrangers, des laboratoires publics ou privés.

Modeling spectral lags in active galactic nucleus flares in the context of Lorentz invariance violation searches

C. Perennes^{1,2,3}, H. Sol¹ and J. Bolmont²

¹ LUTH, Observatoire de Paris, PSL Research University, CNRS, Université Paris Diderot, 5 Place Jules Janssen, F-92190 Meudon, France

² Sorbonne Université, Université Paris Diderot, Sorbonne Paris Cité, CNRS/IN2P3, Laboratoire de Physique Nucléaire et de Hautes Energies, LPNHE, 4 Place Jussieu, F-75252 Paris, France

³ Presently at Università di Padova and INFN, I-35131 Padova, Italy

Not received and not accepted yet.

ABSTRACT

Context. High-energy photons emitted by flaring active galactic nuclei (AGNs) have been used for many years to constrain modified dispersion relations in vacuum encountered in the context of quantum gravity phenomenology. In such studies, done in the GeV-TeV range, energy-dependent delays (spectral lags) are searched for, usually neglecting any source-intrinsic time delay.

Aims. With the aim being to distinguish lorentz invariance violation (LIV) effects from lags generated at the sources themselves, a detailed investigation into intrinsic spectral lags in flaring AGNs above 100 GeV is presented in the frame of synchrotron-self-Compton (SSC) scenarios for their very-high-energy (VHE) emission.

Methods. A simple model of VHE flares in blazars is proposed, allowing to explore the influence of the main physical parameters describing the emitting zones on intrinsic delays.

Results. For typical conditions expected in TeV blazars, significant intrinsic lags are obtained, which can dominate over LIV effects, especially at low redshifts, and should therefore be carefully disentangled from any extrinsic lags. Moreover, two main regimes are identified with characteristic spectral lags, corresponding to long-lasting and fast particle acceleration.

Conclusions. Such intrinsic spectral lags should be detected with new-generation instruments at VHE such as the Cherenkov Telescope Array which begins operation in a few years. This will provide original constraints on AGN flare models and open a new era for LIV searches in the photon sector.

Key words. Radiation mechanisms: non-thermal – Galaxies: active – BL Lacertae objects: general – Astroparticle physics

1. Introduction

Energy-dependent time-lags in signals arriving from remote cosmic gamma-ray emitters are of particular interest both for understanding the physics of astrophysical sources and for investigating possible new phenomena impacting on photon propagation. Lorentz invariance violation (LIV) is an example of such a phenomenon. It appears as a striking outcome of some Quantum Gravity (QG) models in the form of a modified dispersion relation for photons in vacuum and is one of the most explored ways in QG phenomenology (Amelino-Camelia 2013). It is also included as a starting hypothesis in the standard model extension (SME), an effective field theory built from the Lagrangian of the standard model of particle physics including terms for LIV and charge parity time reversal (CPT) violation (Kostelecký & Mewes 2008, 2009).

Although the present paper focuses on spectral lags induced by a LIV effect in the photon sector, it is necessary to stress that these are not the only possible phenomenon arising from LIV that could be measured with astrophysical sources (see Mattingly 2005, for a review). A modified dispersion relation for photons in vacuum can indeed be interpreted as the photon taking a nonzero ef-

fective mass. In that case, normally forbidden processes such as photon decay ($\gamma \rightarrow e^+e^-$) and Cherenkov radiation ($e^- \rightarrow \gamma e^-$) would be allowed in vacuum, and cross-section for the $\gamma_{\text{HE}} + \gamma_{\text{EBL}}$ absorption process of high-energy photons on the extragalactic background light (EBL) would be modified. The latter effect would result in the Universe being more transparent than expected with the standard EBL absorption with no LIV (Biteau & Williams 2015; Tavecchio & Bonnoli 2016; Abdalla et al. 2019). Depending on the QG model considered, it is also possible to obtain vacuum birefringence in addition to energy-dependent speed of light: photons could have different speeds depending on their polarization (Götz et al. 2014; Wei 2019). Several other types of effects are also actively analyzed in the electron sector (Altschul 2005, 2006) and in the gravitational sector (Le Poncin-Lafitte et al. 2016; Bourgoïn et al. 2017; Kostelecký & Mewes 2017). Such LIV effects might further modify the launching mechanism of active galactic nucleus (AGN) jets and the radiative processes involved in the generation of blazar flares, but are neglected in the present work.

The first sources proposed to look for LIV spectral lags were gamma-ray bursts (GRBs) because they could be ob-

47 served at large redshifts and in great numbers by satellites
48 in the soft gamma-ray range (Amelino-Camelia et al. 1998),
49 but flaring AGNs were used almost from the same time
50 (Biller et al. 1999). As in GRBs, AGNs appear to be strong
51 gamma-ray emitters and their active states are observed by
52 detectors with a high effective area such as ground-based
53 Imaging Atmospheric Cherenkov Telescopes (IACTs), with
54 large enough sample sizes to measure fast variability. In
55 addition, AGNs can be monitored regularly and since an
56 AGN flare lasts longer than a GRB, the probability to catch
57 a flare signal under alert is higher. In this regard, blazars
58 emitting in the tera-electronvolt (TeV) range are especially
59 interesting since they are the most variable population of
60 gamma-ray loud AGNs. Their observation with the first
61 generation of IACT, such as Whipple, H.E.S.S., MAGIC,
62 and VERITAS, has already provided stringent limits on
63 spectral time-lags and LIV parameters (Albert et al. 2008;
64 Abramowski et al. 2011, 2015; Zitzer 2013).

65 The performance aimed for CTA, the Cherenkov Tele-
66 scope Array (Acharya et al. 2019), will potentially allow
67 for increasingly significant lag measurements thanks to a
68 larger energy range (20 GeV – 300 TeV), a higher sensitiv-
69 ity ($\times 10$), and a better temporal resolution with respect to
70 the present generation of IACT, and observation strategies
71 designed to optimize the number of transient or variable ob-
72 ject detections. The measured lags, if significant, will have
73 to be interpreted as propagation delays, as effects intrinsic
74 to the sources, or as a superposition of both.

75 The present work is a first attempt to gain knowledge
76 on source-intrinsic spectral lags of flaring AGNs at high and
77 very high energies and on short timescales relevant for LIV
78 searches, using leptonic AGN flare modeling. In this study,
79 only the LIV effect on the propagation of photons in vac-
80 uum and the subsequent time-delays engendered are consid-
81 ered to keep a relatively simple AGN flare model. Section 2
82 presents the general context of the search for LIV signatures
83 from the analysis of blazar gamma-ray flares. We briefly
84 present and apply a standard Synchrotron-Self-Compton
85 (SSC) scenario for such flares in section 3, focusing on pur-
86 pose on the dominant and unavoidable mechanisms needed
87 to generate the burst. We explore the intrinsic SSC time de-
88 lays which are induced in the gamma-ray range in section 4,
89 and further characterize them in section 5. Section 6 focuses
90 on the VHE domain ($E > 100$ GeV) to compare potential
91 intrinsic and LIV time-lags, and further astrophysical issues
92 are discussed. Conclusions and perspectives are presented
93 in section 7.

94 2. Search for Lorentz invariance violation from 95 spectral lags in blazars

96 2.1. Spectral lags and Lorentz invariance violation

97 Focusing on spectral lags in the context of QG phe-
98 nomenology, and neglecting birefringence effects, the mod-
99 ified dispersion relation is usually expressed as

$$E^2 \simeq p^2 c^2 \times \left[1 \pm \left(\frac{E}{E_{QG}} \right)^n \right], \quad (1)$$

100 where c is the low-energy limit of the speed of light, E_{QG}
101 is the energy to be measured or constrained at which LIV

effects should become non-negligible and the sign \pm trans- 102
lates into the possibility to have an increasing (superlumi- 103
nal) or decreasing (subluminal) speed when photon energy 104
increases. The value of E_{QG} is usually expected to be of 105
the order of the Planck scale $E_P \sim 10^{19}$ GeV. Present day 106
IACT experiments probe the linear effect ($n=1$) while the 107
quadratic effect ($n=2$) is still far from reach. However, other 108
orders are investigated at VHE with other experiments (see 109
Kostelecký & Russell 2011, and references therein). More- 110
over, for odd values of n , there is a correspondence be- 111
tween the photon helicity and the subluminal or superlu- 112
minal case. In this first work, we neglect this helicity effect 113
and assume only either the subluminal or superluminal case 114
for odd n values. 115

The use of variable or transient and distant astrophys- 116
ical sources for LIV searches was first proposed in the 117
late 90s (Amelino-Camelia et al. 1998). The modified dis- 118
persion relation of Equation 1 naturally leads to an energy- 119
dependent group velocity of light. Two photons of different 120
energies (E_h and E_l , with $E_h > E_l$), assumed to have been 121
emitted at the same time from the same place by a source 122
at redshift z would be detected with a spectral lag 123

$$\Delta t_{LIV,n} \simeq \pm \frac{n+1}{2} \frac{E_h^n - E_l^n}{E_{QG}^n} \kappa_n(z), \quad (2)$$

where the distance parameter 124

$$\kappa_n(z) = \int_0^z \frac{(1+z')^n}{H(z')} dz' \quad (3)$$

is an increasing function of redshift taking into account 125
Universe expansion during photon propagation (Jacob & 126
Piran 2008). Here, $H(z)$ is the Hubble parameter. It is nec- 127
essary to point out that this expression, although used in 128
all LIV searches performed so far, was obtained under the 129
implicit assumption that translations are not affected by 130
Planck scale effects. Other expressions have been proposed, 131
for example in the deformed special relativity (DSR) ap- 132
proach (see e.g., Rosati et al. 2015). From Equation 2, it 133
is common to express the “time-lag over energy difference” 134
parameter τ_n such that 135

$$\tau_n \equiv \frac{\Delta t_{LIV,n}}{E_h^n - E_l^n}. \quad (4)$$

This parameter is constrained and limits on E_{QG} are de- 136
rived from astrophysical source observations. 137

The lags induced by a LIV effect are expected to be 138
small. Maximizing them requires observation of sources 139
preferably with high redshifts and hard spectra on a wide 140
energy range so that κ_n and $E_h^n - E_l^n$ are maximized. Fast 141
variability is also required in order to measure the lags. 142
The high-energy gamma-ray domain is therefore particu- 143
larly suitable for such studies. 144

The expression of Equation 2 was obtained assuming 145
that high- and low-energy photons are emitted at the same 146
time from the same place, that is, neglecting any source- 147
intrinsic delays possibly resulting from emission mecha- 148
nisms and source extent. In principle, the measured time- 149
lag Δt_m should rather be expressed as the sum of delays 150
with different origins: 151

$$\Delta t_m = \Delta t_{LIV} + (1+z)\Delta t_s + \sum_j \Delta t_j, \quad (5)$$

where Δt_s is the delay due to the emission processes at the source located at redshift z and Δt_j accounts for various additional effects which could affect Δt_m . These terms include for example the dispersion by free electrons along the line of sight, mostly important in the radio range, potential lags due to special relativistic effects in the case where photons have a nonzero rest mass, or lags caused by the gravitational potential integrated from the source to the Earth (see Gao et al. 2015; Wei et al. 2016, and references therein). These extra terms Δt_j are neglected in the present work.

2.2. Intrinsic time-lags from a blazar flare

In the gamma-ray domain, only one flare from Mrk 501 has shown an indication of a 4 ± 1 min time-lag between energy bands below 250 GeV and above 1.2 TeV (Albert et al. 2007). Barely significant spectral lags $\tau_1 = (0.030 \pm 0.012)$ s GeV^{-1} and $\tau_2 = (3.71 \pm 2.57) \times 10^{-6}$ s GeV^{-2} were later reported from the same data set (Albert et al. 2008). This flare, recorded on July 9 2005 by the MAGIC Cherenkov telescopes, suggests that intrinsic delays can exist in AGN flares, while the fact that it is the only one detected implies that intrinsic effects are certainly different for each AGN and perhaps from one flare to another, even in the same source.

Apart from the previous example, no significant spectral lag has ever been measured at GeV and TeV energies from AGNs, and source intrinsic effects have been ignored when constraining the LIV energy scale. Neglecting intrinsic effects could be partially justified when the energy range considered in the analysis is restricted enough to ensure that observed photons can be considered as all emitted together at once in the cosmic source. However, using stringent energy selections has a drawback since it drastically decreases statistics.

Delays can indeed easily appear during the emission of photons from cosmic sources. Such intrinsic spectral time-lags have already been unambiguously detected in some GRBs, and have mostly been reproduced by models considering light-travel-time effects from extended and inhomogeneous emitting zones as expected in standard GRB scenarios (Dai et al. 2017, and references therein). In the case of blazar flares, intrinsic effects do not appear to be as important and have been poorly detected up to now. Nevertheless, they should be detected, either soon with current instruments during some extraordinary flare fully monitored over a large spectral gamma-ray range, or in the coming years with a new generation of instruments providing high-quality light curves and dynamical spectra at VHE. Therefore, in the context of LIV signature searches, intrinsic effects need to be further investigated, at least to help in constraining the QG energy scale in case of future detections of significant time delays in AGN flares (Perennes et al. 2017).

Several time-dependent emission models of nonthermal emission in AGNs have been proposed in the literature, such as for example by Blandford & Königl (1979), Marscher & Gear (1985), Celotti et al. (1991), Böttcher et al. (1997), Katarzyński et al. (2003), Joshi & Böttcher (2011), Lewis et al. (2016). As a matter of fact, such scenarios usually induce possible spectral lags but such intrinsic lags have not been purposefully analyzed in the context of TeV blazar flares. We distinguish here two different types of time de-

lays, the “macroscopic” and the “microscopic” ones, depending on their values and origins.

Macroscopic delays correspond to a variety of long lags induced by the global structure and properties of extended nonhomogeneous emitting zones. Different parts of the source emit in different spectral ranges, therefore inducing possibly important time-lags depending on the specific geometry and kinetics of the radiating plasma. This type of scenario was proposed for instance by Sokolov et al. (2004), while triggering an AGN flare by the collision of a stationary shock wave with a relativistic shock wave in the jet, later forming reverse and forward shocks which both accelerate particles. The complex jet geometry as well as acceleration and emission pattern which then develop can result in long time-lags. This model successfully reproduced a flare observed in 3C 273, in which X-rays were delayed by about one day with respect to their infrared counterparts (Sokolov et al. 2004). Another example of “macroscopic delay” has been obtained by Bednarek & Wagner (2008) who explained the time-lag of about four minutes measured in the 2005 Mrk 501 flare by considering a continuous increase of the global Lorentz factor of the emitting zone propagating along the jet. In such a model of an accelerating blob, with an increase of the Doppler boosting effect, lower-apparent-energy photons are, on average, emitted in a different location from higher-apparent-energy photons, creating the observed spectral time delay.

In the present study we focus on microscopic delays, which are barely discussed at TeV energies although they are easily produced in standard one-zone SSC models and naturally come from the temporal evolution of the distribution of emitting particles. Such microscopic delays have already been analyzed by Lewis et al. (2016) in the context of X-ray variability studies in blazar jets. Focusing on synchrotron emission, these latter authors produced flare light curves and their associated X-ray time-lags. Applying them to data from Mrk 421, they were able to characterize some acceleration parameters in that source. However, Lewis et al. (2016) entirely neglect the inverse-Compton losses which are mandatory to describe gamma-ray time delays. In the following section, we consider a minimal time-dependent leptonic model to generate blazar flares and study short intrinsic time delays at gamma-ray energies, above 1 MeV.

3. Time-dependent model

3.1. Description of the electron distribution

The time evolution of a flare is deduced from the description of the electron population $N_e(\gamma, t)$ at the source in a single homogeneous emitting zone, with $\gamma = E/(m_e c^2)$ being the Lorentz factor of electrons. We adopt the standard SSC scenario presented in Katarzyński et al. (2001, 2003) but simplify the geometry to focus on γ -ray flares arising from a small spherical blob of plasma. Further developments of the simulation codes were done to adapt them to a detailed analysis of spectral lags. The evolution of the electron density is expressed as:

$$\frac{\partial N_e^*(t, \gamma)}{\partial t} = \frac{\partial}{\partial \gamma} \{ [\gamma^2 C_{\text{cool}}(t) - \gamma C_{\text{acc}}(t)] N_e^*(t, \gamma) \}, \quad (6)$$

where C_{cool} accounts for radiative energy losses and C_{acc} for acceleration of electrons or energy gain (neglecting here

272 adiabatic losses). This differential equation admits an analytical
273 solution with an initial electron spectrum $N_e(0, \gamma)$
274 defined as a power law function with a cut-off:

$$N_e(0, \gamma) = K_0 \gamma^{-n} \left[1 - \left(\frac{\gamma}{\gamma_{c,0}} \right)^{n+2} \right], \quad (7)$$

275 where K_0 is the electron density at $\gamma = 1$, n the electron
276 spectrum index, and $\gamma_{c,0}$ the cut-off energy.

277 The coefficient C_{cool} takes into account the SSC energy
278 losses and can be expressed as follows:

$$C_{\text{cool}}(t) = \frac{4\sigma_T (U_B(t) + U_r(t))}{3m_e c}, \quad (8)$$

279 where the first term corresponds to synchrotron energy
280 losses, with $U_B(t) = B(t)^2/8\pi$ being the magnetic field
281 energy density, and the second term is related to the
282 inverse-Compton (IC) energy losses on the synchrotron
283 photon field, corresponding to the synchrotron energy density
284 $U_r(t)$. It is parameterized as:

$$U_r(t) = U_B(t)/\eta. \quad (9)$$

285 This choice allows us to simplify the resolution of Equation
286 6, which then admits an analytical solution, and to decrease
287 the computation time significantly. The η parameter
288 represents the relative importance between the synchrotron
289 and IC radiative cooling. It has to be constant over time or
290 to be large enough in order for the analytic solution to be
291 valid. This limits the parameter space that can be explored
292 to the one corresponding to synchrotron-dominated sources
293 like high-frequency peaked BL Lac (HBL) objects.

294 We further assume a characteristic time t_0 for the temporal
295 evolution of the main flare parameters. This time is
296 typically related to the speed of sound in a blob of relativistic
297 plasma characterized by a radius R_0 as $t_0 = R_0/(c\sqrt{3})$,
298 c being the speed of light in vacuum. The evolution of the
299 magnetic field strength is then described as:

$$B(t) = B_0 \left(\frac{t_0}{t} \right)^{m_b}, \quad (10)$$

300 with B_0 being the initial value of the magnetic field at t_0 ,
301 and m_b its temporal evolution index.

302 Finally, C_{acc} corresponds to the acceleration processes
303 and allows us to initiate the flare starting from low states
304 of the electron spectrum distribution. It is expressed as:

$$C_{\text{acc}}(t) = A_0 \left(\frac{t_0}{t} \right)^{m_a}, \quad (11)$$

305 where A_0 is the initial acceleration amplitude, and m_a the
306 acceleration temporal index.

307 3.2. Spectral energy distribution

308 Spectral energy distributions (SEDs) are generated assuming a
309 SSC emission model. To compute the SSC radiation, we use standard
310 packages described in Katarzyński

et al. (2001) which provide the synchrotron and IC emission
311 from a given electron spectrum, taking into account
312 synchrotron self absorption of the emitting zone. Absorption
313 from the extragalactic background light (EBL) is included
314 following the model of Franceschini et al. (2008).
315 The evolution of the electron spectrum and of the SED is
316 shown in Figure 1 for the set of parameters given in Table 1.
317 Such physical parameters correspond to standard values as
318 previously deduced with the same SSC packages and others
319 for the archetypal TeV sources Mrk 501, Mrk 421, and PKS
320 2155-304 (Katarzyński et al. 2001, 2003; Abramowski et al.
321 2012) and can be considered as typical values expected in
322 blazar flares. This explains the small redshift value adopted
323 here, leading to a low EBL absorption. 324

SSC Parameter	Value	Unit
δ	40	
B_0	65	mG
R_0	5×10^{15}	cm
K_0	300	cm^{-3}
γ_{cut}	4×10^4	
n	2.4	
z	0.03	
Evolution parameter	Value	Unit
A_0	4.5×10^{-5}	s^{-1}
m_a	5.6	
m_b	1	

Table 1. Standard parameters expected in typical blazar TeV
flares, considered as the first reference set throughout this paper.

3.3. Light curve determination

325 To compute the light curves at different energies, the
326 SEDs are integrated over the required energy bands, each
327 SED giving one flux point for each light curve. Examples
328 of flare light curves are shown in Figure 2 (left and center)
329 for parameters of Table 1. In order to consider only realistic
330 light curves that may be observed, a selection cut is
331 applied on them. Only light curves with a maximum flux
332 above $2 \times 10^{-15} \text{ cm}^{-2} \text{ s}^{-1}$ are kept. The time t_{max} shown
333 on the light curve is defined from Figure 1 as the time when
334 electrons reach their maximum energy $\gamma_{\text{max}} = \text{max}(\gamma_c(t))$.
335 This time indicates when the radiative cooling timescale
336 becomes shorter than the acceleration timescale, for the
337 most energetic electrons with an energy close to γ_{max} . For
338 this set of parameters, the time t_{max} happens after all the
339 light curves peak, meaning that the electron acceleration
340 timescale is still shorter than the electron cooling timescale
341 for all energies. As a result, the decaying light curves can
342 only be explained by the decrease of the magnetic field. An
343 opposite case can be defined when t_{max} happens before all
344 the light curves peak as shown in Figure 3 (left and center).
345 This case is obtained from the first reference set of
346 parameters increasing the radiative cooling power. This is
347 achieved by changing the B_0 value from 65 mG to 90 mG,
348 and provides us with our second reference set of parameters
349 throughout this paper. Conversely to the previous case,
350

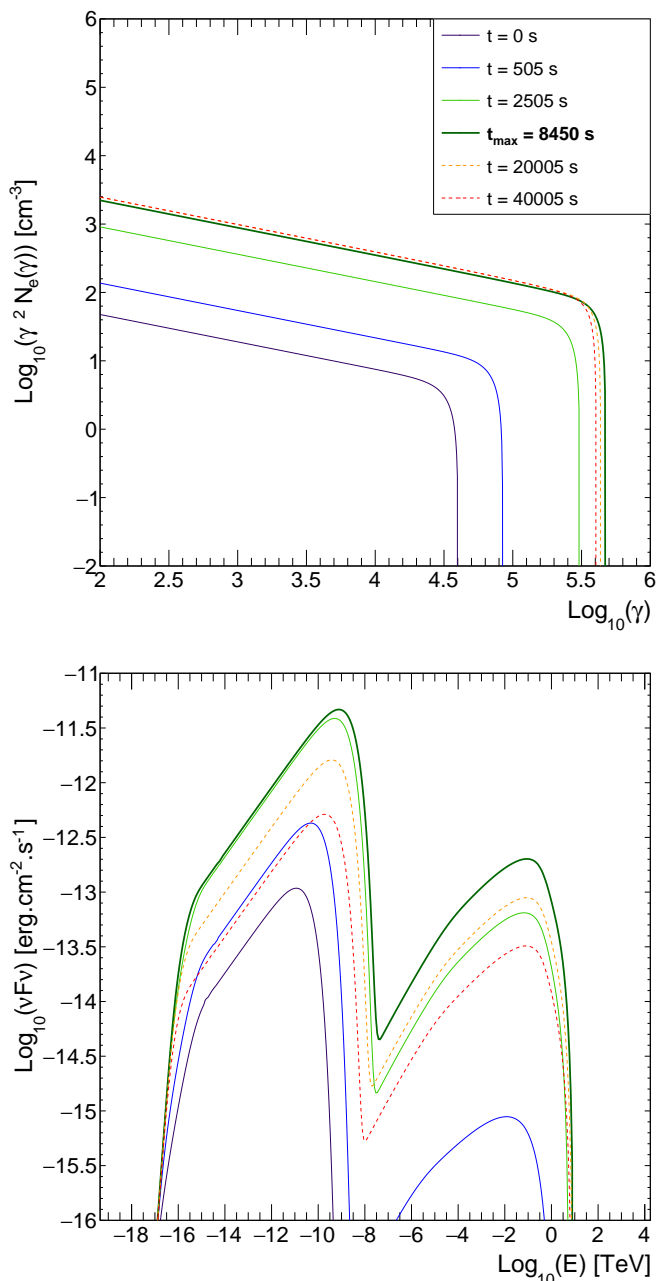


Fig. 1. Electron spectrum (top) and SED (bottom) evolution for the reference set of parameters given in Table 1, illustrating a typical TeV blazar flare. The two plots share the same color code. The full lines correspond to the rising phase of the flare and the dashed lines to its decay. The time t_{max} is defined as the time when the highest energy value $\gamma_{max} = \max(\gamma_c(t))$ is reached in the electron spectrum. The corresponding electron spectrum and SED are plotted in thick lines. The electron spectrum and SED at the maximum luminosity of the flare are not displayed because they almost coincide with the ones at t_{max} for this reference set of parameters.

351 the radiative cooling contributes to the light-curve decay,
 352 resulting in the fact that the most energetic light curves
 353 decay first.

4. Study of time delays

354

4.1. Time delay determination

355

The time delay is determined by computing the time 356
 difference between the maximum of the light curve at the 357
 energy considered and the maximum of the lowest-energy 358
 light curve (1.0-1.8 MeV). A positive lag corresponds to the 359
 case when high-energy light curves peak after the lowest- 360
 energy ones. This method, later called the peak position 361
 method (PPM), is rather simplistic but provides a simple 362
 and robust estimation of the time delay, with an accuracy 363
 directly related to the time step chosen for the light curves. 364
 A cross-correlation function (CCF) from Edelson & Krolik 365
 (1988) was also considered but was found to **wrongly re-** 366
construct the time delay in the case of light curves with 367
 varying widths. A comparison of the PPM and CCF is 368
 shown in Figure 4. Two light curves are simulated with a 369
 similar shape as the light curves obtained from the model, 370
 approximated by an asymmetric Gaussian function. A delay 371
 of 800 s is applied to one of the light curves. The width 372
 of the lagged light curve is then varied with respect to the 373
 other one and the PPM and CCF methods are applied to 374
 reconstruct the lag. The CCF is not able to reconstruct the 375
 injected delay as the width difference increases, and more 376
 generally in case the shape of the two light curves is differ- 377
 ent. Concerning the light curves from the model, this point 378
 is further discussed in Section 6.3. 379

4.2. Main results: two time-delay regimes

380

The time delays obtained for the two reference sets of 381
 parameters shown in Figure 2 (right) and Figure 3 (right) 382
 highlight two different time-delay regimes found with the 383
 adopted SSC flare model. These two regimes can be better 384
 characterized by considering whether the time t_{max} is 385
 reached before or after the peaks of the light curves. The 386
 vertical error bars on the time-delay measurement is of 5 s 387
 and the horizontal ones for the energy correspond to the 388
 light-curve energy ranges. 389

In the first case (Figure 2), all the light curves peak be- 390
 fore t_{max} . Thus, the acceleration timescale is shorter than 391
 the cooling one when the flare decays. Electrons are still ac- 392
 celerated and their maximum energy still increases after the 393
 low-energy light curves peak. The decay of the flare is then 394
 induced by the decrease of the magnetic field $B(t)$. Hence, 395
 the increase of the time delay above 1 GeV is explained by 396
 the time required for electrons to be accelerated up to γ_{max} 397
 and to emit the highest-energy photons. Conversely, below 398
 1 GeV, the energy necessary to emit lower-energy photons 399
 is quickly reached by electrons. This leads to a decrease of 400
 the time delay, the low-energy light curves decaying due 401
 to the combined action of the energy-dependent radiative 402
 cooling and of the magnetic field decrease. In the following, 403
 this type of time delay evolution, with a decreasing time de- 404
 lay at low energies and an increasing one at high energies, 405
 is described as an "acceleration -driven regime" because of 406
 the origin of the high-energy delays. 407

In the second case (Figure 3), t_{max} is reached before 408
 the peaks of the light curves, and the energy losses by radi- 409
 ative cooling are soon larger than the energy gains by 410
 acceleration. The decay of the flare is then mostly due to 411
 the radiative cooling. This is achieved by assuming a higher 412
 magnetic field strength initial value ($B_0 = 90$ mG) relative 413

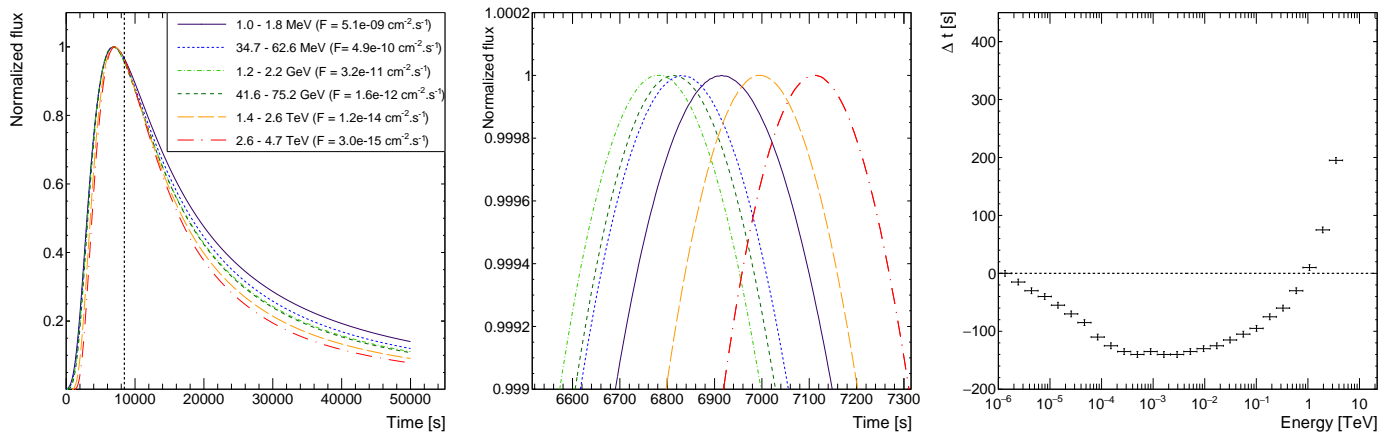


Fig. 2. Normalized light curves (left), zoom close to the light-curve maxima (center), and time-delays between each light curve and the one in the range 1-1.8 MeV (right) obtained for the first reference set of parameters. The vertical dashed line on the light curves (left) corresponds to the time when electrons reach their maximum energy γ_{max} and shows the moment when energy losses dominate over the acceleration at the energy γ_{max} .

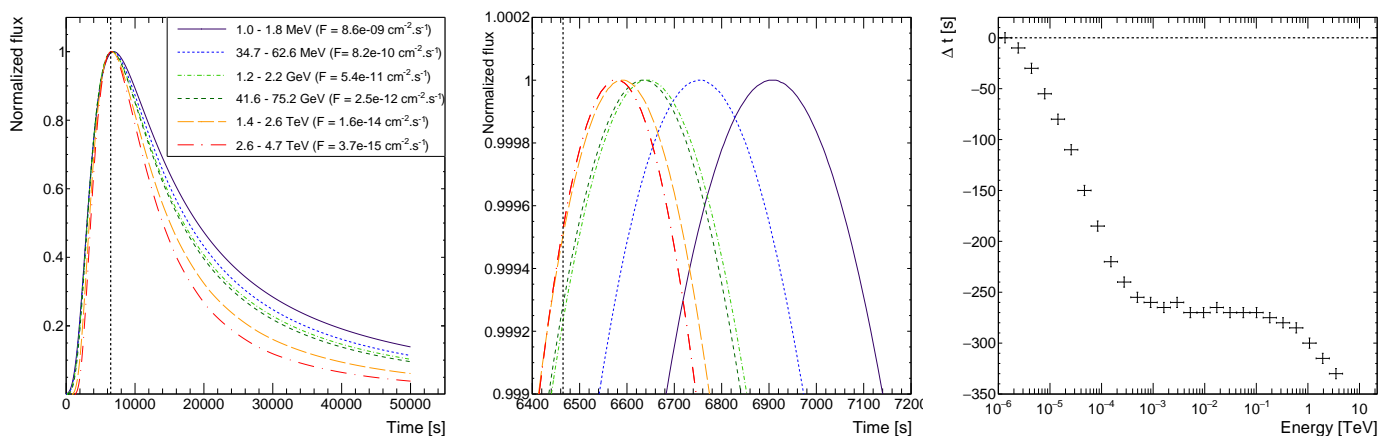


Fig. 3. Normalized light curves (left), zoom close to the light curve maxima (center), and time-delays between each light curve and the one in the range 1-1.8 MeV (right) obtained for the second reference set of parameters (i.e., with $B = 90$ mG). The vertical dashed line on the light curves (left and middle) corresponds to the time when electrons reach their maximum energy γ_{max} and shows the moment when energy losses dominate over the acceleration at the energy γ_{max} .

414 to the previous case, which enhances the electron radiative
415 energy losses. As a consequence, the highest-energy light
416 curves decay first due to a shorter cooling timescale, ex-
417 plaining the decreasing time delay above GeV energies. At
418 lower energies, the cooling timescale of the electrons and
419 the decreasing time delay appear similar to the previous
420 case and due to the combined action of the magnetic field
421 decrease and of the energy-dependent radiative cooling. In
422 the following, such a case with time delays continuously
423 decreasing are described as the "cooling driven regime" be-
424 cause of the main origin of the time delays above GeV en-
425 ergies.

426 The analysis presented in the following section confirms
427 the existence of these two time-delay regimes over a large
428 domain of parameters.

429 5. Influence of model parameters on time delays

430 To investigate the impact of the model parameters on
431 the time delays, each of them is individually varied around
432 the reference values defined in Table 1, namely B_0 , m_b ,
433 A_0 , m_a , δ , $\gamma_{c,0}$ and n . All these values are chosen within a

reasonable range for blazar modeling and also in the domain 434
of validity of our model. Magnetic fields being a key driver 435
for nonthermal blazar emission and SSC electron radiation, 436
several values of B_0 are first explored and then each other 437
parameter is investigated for $B_0 = 65$ mG and $B_0 = 90$ mG 438
respectively. 439

440 5.1. Initial magnetic field strength variations

The magnetic field directly influences the cooling 441
timescale of electrons. Therefore, it contributes to the max- 442
imum energy γ_{max} reached by electrons, meaning that B_0 443
is one of the main parameters acting on the intrinsic time 444
delays. 445

Several values of B_0 are used to evaluate the influence 446
of the magnetic field on the time-delay evolution, ranging 447
from 50 mG to 110 mG. The resulting time delay is shown in 448
Figure 5 as a function of energy. In the low-energy domain, 449
for $E \lesssim 1$ GeV, the time delay does not qualitatively change 450
with B_0 although it slightly decreases as B_0 increases due to 451
a stronger radiative cooling. Conversely at high energies, for 452
 $E \gtrsim 1$ GeV, the variation of the initial magnetic field value 453

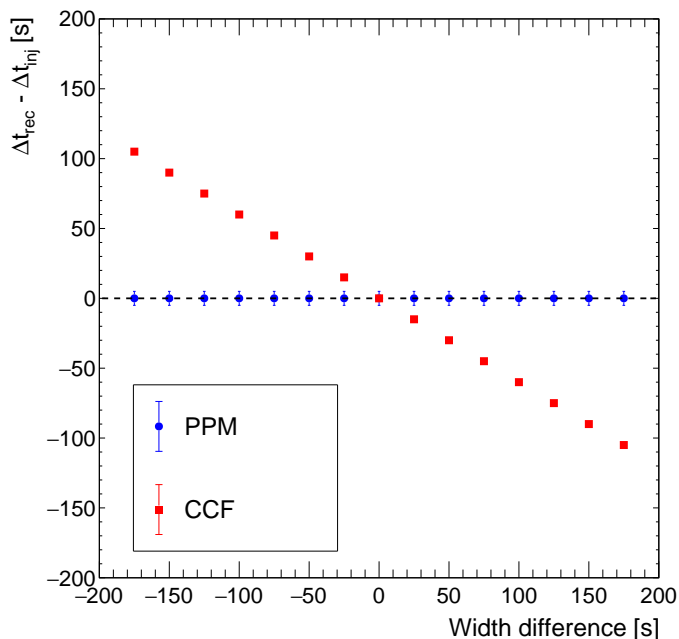


Fig. 4. Time delay measured with PPM and CCF between two simulated asymmetric Gaussian light curves varying the width of one of them. The injected delay value is fixed at $\Delta t_{inj} = 800$ s. The measurement from the CCF shows a misreconstruction of the injected time delay as the width difference increases. The asymmetric Gaussian function used has $\sigma_{left} = 2500$ s and $\sigma_{right} = 20000$ s.

induces large variations of the time delay and a significant change of its behavior, with a transition zone around 80 mG from an increasing to a decreasing phase when B_0 increases. Within this transition, some cases show an almost constant time delay relative to the MeV light curve, which means that they present just very small or even no relative time delay in the limited energy range from 1 GeV to 1 TeV.

5.2. Magnetic field temporal index

As defined in Equation 10, the magnetic field strength is assumed to decrease over time with an index m_b . A value $m_b = 1$ was found adequate to reproduce flares observed in Mrk 421 within the SSC scenario adopted here (Katarzyński et al. 2003), and $m_b = 2$ corresponds for instance to the case of magnetic flux conservation in a blob propagating along a quasi-conical jet. Here, the index m_b is varied from 1 to 2 and time delays are shown for the two reference cases in Figure 6.

Starting from an acceleration-driven regime in the case where $B_0 = 65$ mG, an overall increase of the time delay value is observed. For $E \gtrsim 1$ GeV the time delay evolution does not qualitatively change and lags always increase. For $E \lesssim 1$ GeV, the time delay decreases less and less as m_b increases and finally evolves towards only increasing time delay. This transition is explained by the rapid decrease of the magnetic field which induces low-energy flares quickly decaying while electrons are still accelerating. As a consequence, the highest-energy light curves peak at later times due to the time needed for the electrons to reach high γ values.

Starting from a cooling driven regime in the case where $B_0 = 90$ mG, increasing m_b induces a transition to the acceleration-driven regime. In those cases, the rapid decrease of $B(t)$ reduces the radiative cooling power. Hence the acceleration time scale becomes shorter than the radiative cooling timescale, thus shifting t_{max} to later times. When m_b is larger, the highest-energy light curve peaks later while the faster magnetic field decrease induces the lowest-energy light curves to decay earlier.

5.3. Doppler factor variations

A modification of the Doppler factor δ does not change the temporal evolution of the source in its own frame and simply implies a change on the Doppler boosting effect for the observer leading to variations of the observed variability due to time contraction as well as variations of the observed flux and energy. The energy-dependent time delay for different δ ranging from 20 to 50 is shown in Figure 7 for the two regimes. The dominant effect on the time-delay evolution is the time contraction, inducing smaller observed time delays as δ becomes larger. In reality, the time delays obtained for different δ values appear almost proportional to each other by the ratio of their Doppler factor, as shown for instance for $B_0 = 90$ mG by the delay at 1 TeV for $\delta = 40$ and $\delta = 20$ which gives $\Delta t_{\delta=40}(1 \text{ TeV}) \simeq 293$ s and $\Delta t_{\delta=20}(1 \text{ TeV}) \simeq 600$ s, with a ratio approximately equal to the Doppler factor ratio. However, it can also be noted that the variation of the maximum energy considered for the time-delay computation is an effect of the Doppler boosting on the apparent flux value. This is a consequence of our choice to neglect light curves with flux values below $2 \times 10^{-15} \text{ cm}^{-2} \text{ s}^{-1}$. Also, the energy shift due to Doppler boosting can lead to a change of the time delay sign which

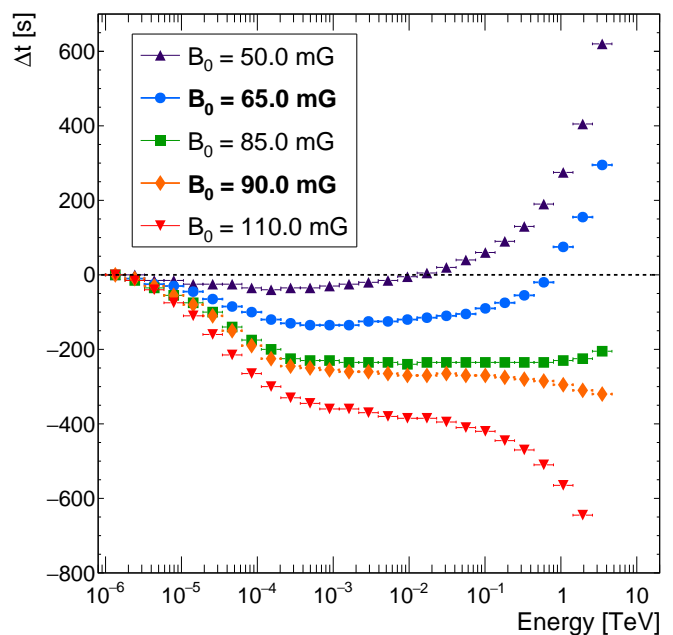


Fig. 5. Time delay vs. energy for different B_0 values. The two cases in bold in the legend correspond to the ones discussed in Section 4.2. All other parameters have the values given in Table 1.

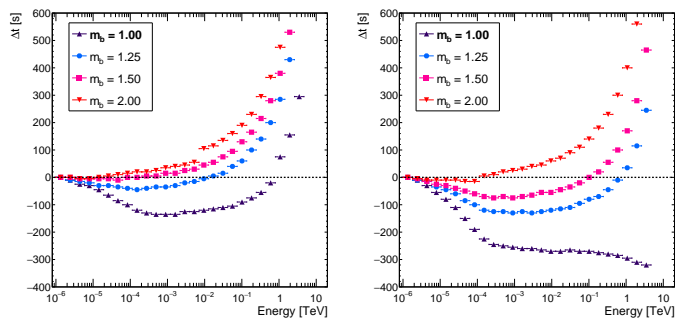


Fig. 6. Time delay vs. energy for different magnetic field evolution index m_b with $B_0 = 65$ mG (left) and $B_0 = 90$ mG (right). All other parameters are unchanged (Table 1). The two cases in bold in the legend correspond to the situation discussed in Section 4.2.

515 is not expected from the time contraction alone as seen for
516 $B_0 = 65$ mG at $E \approx 1$ TeV.

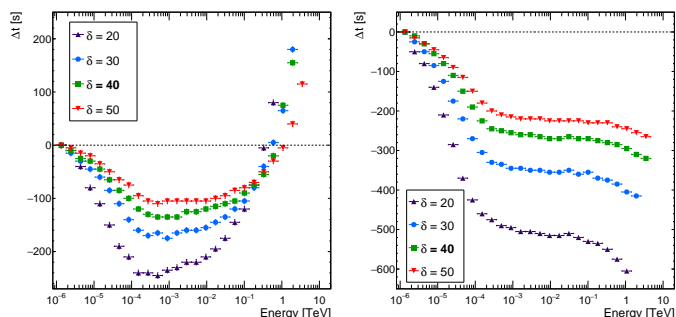


Fig. 7. Time delay vs. energy for different Doppler factor δ values with $B_0 = 65$ mG (left) and $B_0 = 90$ mG (right). All other parameters are unchanged (Table 1). The two cases in bold in the legend correspond to the situation discussed in Section 4.2.

517 5.4. Acceleration parameter variations

518 The acceleration term, defined in Equation 11, depends
519 on two parameters, namely the initial amplitude A_0 and the
520 evolution index m_a . Varying the acceleration parameters
521 modifies the electron acceleration time scale and thus the
522 time t_{max} with respect to the flare maxima. This can in turn
523 induce a transition between the two time-delay regimes.

524 The time delay obtained for different A_0 values ranging
525 from $4.0 \times 10^{-5} \text{ s}^{-1}$ to $6.0 \times 10^{-5} \text{ s}^{-1}$ is shown in Figure 8.
526 In the case where $B_0 = 65$ mG, decreasing A_0 increases the
527 time delays for the highest energies. The acceleration power
528 is weaker and high-energy electrons need more time to reach
529 γ_{max} . In addition, the maximum electron energy γ_{max} is
530 smaller, implying a weaker cooling effect which shifts t_{max}
531 to later times. With larger A_0 values, a transition between
532 the two regimes occurs, leading to a cooling-driven regime.
533 The acceleration is then stronger involving a higher γ_{max}
534 value, inducing a stronger cooling effect for the most ener-
535 getic electrons. Hence, increasing A_0 brings electrons much
536 faster to higher γ_{max} values which then quickly suffer from
537 intense radiative energy losses, entering into the cooling-
538 driven regime.

539 Conversely, starting from a cooling-driven regime with
540 $B_0 = 90$ mG, the opposite situation occurs with a transition

541 to the acceleration-driven regime when A_0 decreases. Small
542 A_0 values induce longer acceleration timescales and lower
543 γ_{max} values, the cooling power at γ_{max} becomes weaker,
544 electrons need a long time to reach their maximum energy,
545 the t_{max} is shifted to later times, and a transition occurs
546 to the acceleration-driven regime when A_0 is small enough.
547 On the other hand, larger A_0 values imply a shorter accel-
548 eration timescale, γ_{max} is reached at earlier times, and the
549 cooling power becomes stronger. Then the highest-energy
550 light curves reach their peaks much earlier than the refer-
551 ence case, which explains the negative time delays.

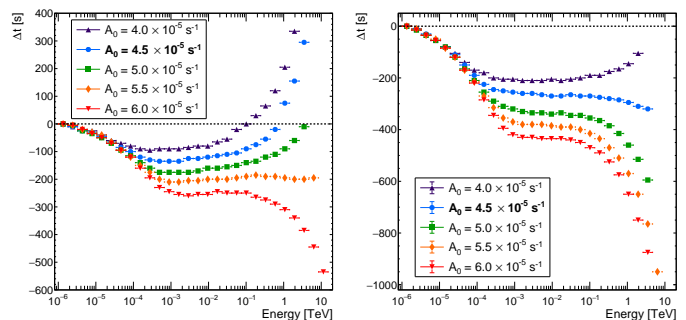


Fig. 8. Time delay vs. energy for different acceleration amplitude A_0 values with $B_0 = 65$ mG (left) and $B_0 = 90$ mG (right). All other parameters are unchanged (Table 1). The two cases in bold in the legend correspond to the situation discussed in Section 4.2.

552 Similar reasoning applies to the acceleration evolution
553 index parameter m_a (Figure 9), varied from 4.5 to 5.9. In-
554 creasing m_a induces longer acceleration timescales. How-
555 ever, the variation of m_a does not lead to a significant
556 change of regime. For $B_0 = 90$ mG, a hint of transition
557 is observed for large m_a values when the acceleration is
558 weaker. For $B_0 = 65$ mG, the overall delay decreases to-
559 ward negative values for a stronger acceleration when m_a
560 decreases.

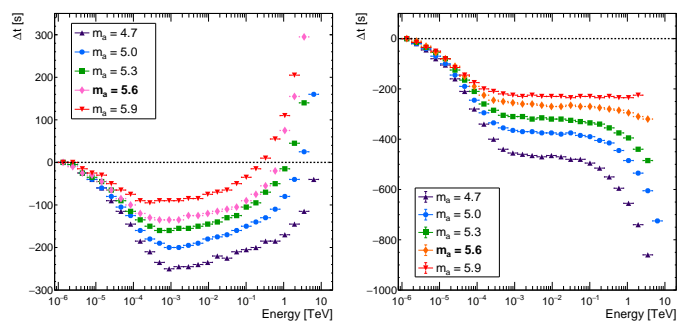


Fig. 9. Time delay vs. energy for different acceleration evolution m_a values with $B_0 = 65$ mG (left) and $B_0 = 90$ mG (right). All other parameters are unchanged (Table 1). The two cases in bold in the legend correspond to the situation discussed in Section 4.2.

561 5.5. Initial electron distribution index variations

562 The initial electron spectrum assumed in the present
563 flare scenario follows a power law function with a high-
564 energy cut-off (Equation 7). The initial electron density K_0
565 is only a scaling parameter and does not affect the time

566 evolution. In the transfer equation, modifying n does not
 567 change the balance between electron acceleration and cool-
 568 ing effects and in practice γ_{max} and t_{max} remain at the
 569 same values when n changes. However, the initial electron
 570 spectrum index n impacts the ratio of low- to high-energy
 571 electrons, with a higher proportion of lower-energy elec-
 572 trons for high n values.

573 The time delays obtained with values from $n = 2.2$ to
 574 $n = 2.8$ are presented in Figure 10. For $B_0 = 90$ mG, start-
 575 ing from a cooling-driven regime, a transition occurs to the
 576 acceleration-driven regime when n decreases. Such a transi-
 577 tion can be easily explained because the flare is globally
 578 shorter when n is smaller while t_{max} remains the same
 579 whatever the value of n . This is the consequence of the
 580 fact that the electron population is on average more ener-
 581 getic for smaller n , therefore inducing light curves which
 582 peak at earlier times. The transition occurs when n is small
 583 enough to produce light curves peaking earlier than t_{max} .
 584 For $B_0 = 65$ mG, the variations of the time delay are small
 585 and do not really highlight the influence of the param-
 586 eter n , however the evolution of the time delay follows the
 587 same behavior. A smaller n value induces an overall shorter
 588 flare, with light curves peaking at earlier times because they
 589 are produced by a more energetic electron population. The
 590 maxima of the light curves become shifted at earlier times
 591 than t_{max} thus inducing larger delays for the highest-energy
 592 light curves.

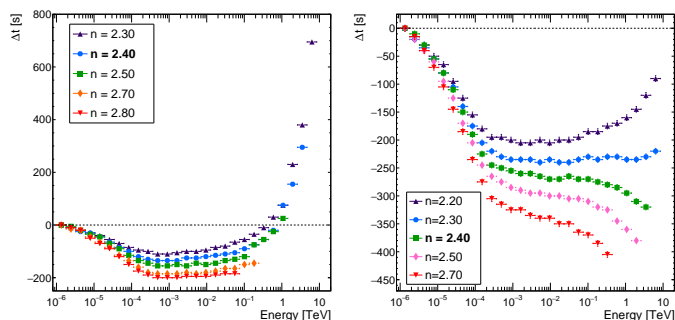


Fig. 10. Time delay vs. energy for different initial electron index n values with $B_0 = 65$ mG (left) and $B_0 = 90$ mG (right). All other parameters are unchanged (Table 1). The two cases in bold in the legend correspond to the situation discussed in Section 4.2.

593 5.6. Energy break of electron distribution evolution

594 The energy cut-off $\gamma_{c,0}$ defines the maximum energy of
 595 electrons at the starting time t_0 (Equation 7). Using lower
 596 values of $\gamma_{c,0}$ than 4×10^4 increases the time needed for
 597 electrons to reach their highest energy γ_{max} . For higher
 598 $\gamma_{c,0}$ values, electrons are quickly accelerated to high γ
 599 values and γ_{max} become larger leading to a shorter cooling
 600 timescale. The resulting time delays for $\gamma_{c,0}$ ranging from
 601 2×10^4 to 8×10^4 are shown in Figure 11 for the accelera-
 602 tion- and cooling-driven cases.

603 For $B_0 = 65$ mG, decreasing $\gamma_{c,0}$ leads to an increase of
 604 the time delay values for all energies. Indeed, starting from
 605 less energetic electrons implies that they need more time to
 606 be accelerated up to γ_{max} , thus shifting the highest-energy
 607 light curves to later times. For larger $\gamma_{c,0}$ values, the elec-
 608 tron population is more energetic at t_0 and reaches a larger
 609 γ_{max} within a smaller time t_{max} . In this situation, the cool-

ing timescale becomes shorter at γ_{max} leading to a transi- 610
 tion from the acceleration- to the cooling-driven regime. For 611
 $B_0 = 90$ mG, a similar behavior appears. 612

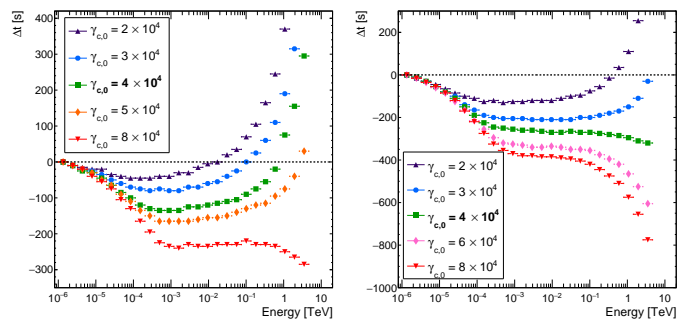


Fig. 11. Time delay vs. energy for different initial maximum energy for electron $\gamma_{c,0}$ values with $B_0 = 65$ mG (left) and $B_0 = 90$ mG (right). All other parameters are unchanged (Table 1). The two cases in bold in the legend correspond to the situation discussed in Section 4.2.

6. Discussion and astrophysical issues 613

614 With the flare model presented here, all the cases inves-
 615 tigated reveal the presence of an energy-dependent intrinsic
 616 time delay at gamma-ray energies. Two distinct regimes,
 617 referred to as “cooling driven” and “acceleration driven”
 618 are found for the time delays, corresponding to the mech-
 619 anism driving the electron evolution when the light curves
 620 peak and the flare starts to decay. In addition, some spec-
 621 ific cases corresponding to the transition between the two
 622 regimes show no delay between roughly 100 GeV and a few
 623 TeV. Adiabatic effects due to the expansion of the emit-
 624 ting zone can affect the quantitative values of time delays
 625 but do not qualitatively modify the global picture. When
 626 added in the differential equation describing the evolution
 627 of electrons (Equation 6), they contribute to reducing the
 628 acceleration term, therefore pushing the system towards the
 629 acceleration-driven regime, which will be reached or not de-
 630 pending on the given set of parameters.

6.1. Observational constraints on the model 631

632 The information on the energy-dependent time delay
 633 can be used in order to constrain the model parameters.
 634 Indeed, if the evolution of the measured time delay corre-
 635 sponds to one of the two regimes, the other one is obviously
 636 ruled out. Clearly, the time delay is a new observable which
 637 can be used to constrain the modeling of blazars.

638 For instance, the observation of a flare from the blazar
 639 Markarian 501 in 2005 (Albert et al. 2007) revealed a
 640 nonzero time delay in the VHE range, the unique case of de-
 641 tection of a time delay at VHE from a blazar. The authors
 642 found a time delay increasing with the energy which ap-
 643 pears to correspond to an acceleration-driven regime. This
 644 suggests a qualitative scenario with a flare initiated through
 645 a sudden shock acceleration or magnetic reconnection in
 646 the emitting zone, immediately followed by a mechanism
 647 inducing the flare decay such as the decrease of the mag-
 648 netic field (or adiabatic expansion). In parallel, accelera-
 649 tion processes are still more efficient than the radiative cool-
 650 ing at the highest energies and thus ensure the observed
 651 acceleration-driven regime.

652 However, most of the blazar flare observations do not
653 show any significant time delays. One example is provided
654 by the exceptional flare of PKS 2155-304 observed by
655 H.E.S.S. in 2006. A CCF was applied to the light curves
656 (Aharonian et al. 2008) between 400 and 800 GeV and
657 above 800 GeV, and no significant delay was found in the
658 data. The reason for such missing time-lags is not clear,
659 because basic SSC flare models such as the one presented
660 here predict significant intrinsic delays. Obviously this can
661 be due to the limited number of observed blazar TeV flares,
662 the poor time coverage and time accuracy, and the limited
663 spectral range of the present data sets. The next generation
664 of gamma-ray instruments should clarify this issue by
665 measuring significant time delays and providing new and
666 precise quantitative constraints on VHE flare models. Indeed,
667 a flare which can only decay through radiative cooling
668 leads inevitably to a cooling-driven regime. Therefore, for
669 example, if future observations of blazar flares do not reveal
670 the presence of time delays decreasing with the energy at
671 VHE, the simplest scenarios with a fast acceleration (or
672 injection) followed by radiative cooling in otherwise constant
673 emitting zone and magnetic field could be excluded. Alternatively,
674 it is also possible that basic SSC scenarios do not
675 describe blazar flares in full details. If time delays are not
676 at all observed at the VHE, then the majority of flares may
677 occur in a specific domain of parameters corresponding to
678 the transition zone between the two time-delay regimes we
679 have identified. This would suggest a physical link and a
680 fine-tuning between acceleration and cooling processes in
681 the global evolution of the flares.

682 6.2. Focus on time delays at very high energies

683 For the search of LIV signatures with IACT, studies
684 are performed in the VHE range only. The intrinsic delays
685 obtained in Sections 4 and 5 are therefore re-calculated here
686 relative to a reference light curve at higher energies, in the
687 range from 42 to 74 GeV which is now used as the zero
688 origin for the delays. Comparing the energy dependency of
689 the intrinsic time delays with the LIV ones can then provide
690 direct constraints on specific QG models since for instance
691 some models produce only one specific type of time delay
692 such as Amelino-Camelia et al. (1997) or Ellis et al. (2000)
693 with positive, linear, energy-dependent delays.

694 To quantify the energy dependency of the intrinsic delays,
695 they are adjusted with a power law function similar to the one
696 used for LIV studies, namely

$$697 \Delta t = \xi \times (E_i^\alpha - E_0^\alpha), \quad (12)$$

698 where α is the energy dependency index, ξ the amplitude
699 of the delay in s $\text{TeV}^{-\alpha}$, and E_0 the midpoint of the energy
700 range of the reference light curve (58.5 GeV). The α and
701 ξ parameters obtained from fitting the time delay for the
702 cases with different B_0 values are shown in Table 2 and for
703 all other cases in Table A.1 of the Appendix. At the transition
704 between the two regimes, α cannot be evaluated since there
705 is no significant time delay. In addition, some cases are
706 not able to produce a significant flare above 250 GeV,
707 implying a poor energy coverage and preventing any estimation
708 of the α parameter. Overall, the energy evolution index
709 α for the cases producing significant time delays is found
to be in the range [0.45 – 0.85].

710 As a consequence, energy-dependent intrinsic time de-
711 lays obtained from the basic SSC flare model described here
712 evolve with an index α different from the QG model pre-
713 dictions from Amelino-Camelia et al. (1997) and Ellis et al.
714 (2000) where $\alpha_{LIV} = 1$. This result illustrates how time-
715 dependent blazar flare scenarios can be used to test these
716 two QG models or any other model predicting a LIV delay
717 with an energy dependency outside the range of values
718 found for the α parameter. Indeed, if a specific QG model
719 predicts a LIV energy-dependent delay with an index α_{LIV}
720 outside this range, the two delays can be discriminated and
721 the QG model can be constrained. Otherwise, the LIV and
722 intrinsic delays are mixed together and remain difficult to
723 disentangle.

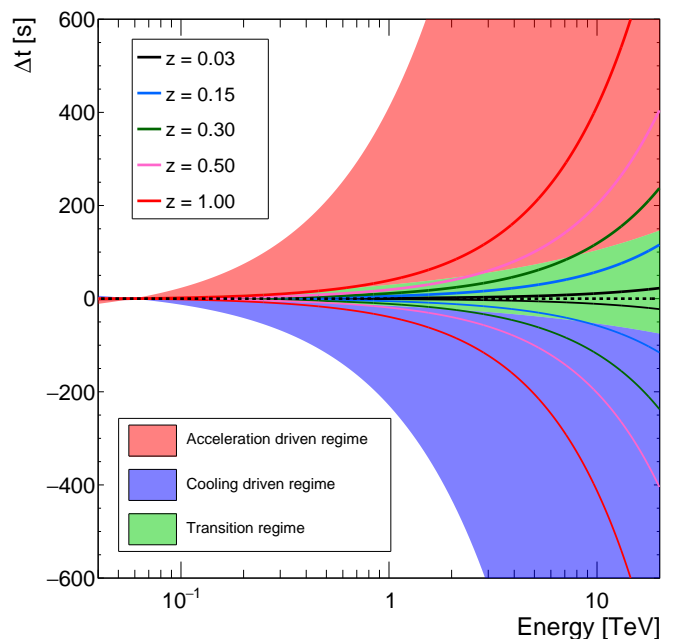


Fig. 12. Typical time delays obtained from the SSC flare model (shaded area) and expected from a linear LIV effect with an energy scale at the Planck energy (full lines) with the redshift evolution found in Jacob & Piran (2008). Other formalism such as DSR would lead to different values but of the same order of magnitude. The dashed line corresponds to $\Delta t = 0$. Positive and increasing LIV delays correspond to subluminal LIV effects, negative and decreasing ones to superluminal LIV effects.

724 To summarize, Figure 12 shows the domain of intrinsic
725 time delays generated in the two regimes and a linear LIV
726 delay at the Planck energy scale ($E_{QG} \sim 10^{19}$ GeV) for
727 subluminal and superluminal effects at different redshifts
728 adopting the redshift evolution from Jacob & Piran (2008).
729 A direct comparison can be done since the redshift does
730 not affect the time-delay evolution with energy but only
731 the observed flux due to the distance and EBL attenuation.
732 Generally speaking, intrinsic time delays appear to be much
733 larger than expected LIV delays in the linear case, except
734 for very large redshifts where observations at VHE remain
735 difficult due to EBL absorption. For higher values of E_{QG} ,
736 the LIV delay will simply become smaller. In the quadratic
737 case, LIV delays will always be much smaller than intrinsic
738 ones and very difficult to disentangle.

B_0 [mG]	ξ [s TeV $^{-\alpha}$]	α
50	274 ± 36	0.64 ± 0.1
60	217 ± 30	0.60 ± 0.1
65	175 ± 23	0.72 ± 0.1
70	128 ± 18	0.61 ± 0.1
80	50 ± 9	0.64 ± 0.2
85	-	-
90	-29 ± 8	0.57 ± 0.2
100	-125 ± 20	0.53 ± 0.1
110	-181 ± 23	0.68 ± 0.1

Table 2. Energy dependent intrinsic time-delay amplitude ξ and power index α for various initial magnetic field strengths in the GeV-TeV energy range. The missing values (shown with a dash) could not be evaluated because there was no significant delay in the considered energy range ($\xi \approx 0$).

6.3. Temporal evolution

A characteristic feature of intrinsic delays is that their magnitude can vary in time during a flare while LIV delays stay constant. This is another observational signature which can provide important information on the origin of the delays. In their study of X-ray variability of blazar flares, Lewis et al. (2016) performed a Fourier transform analysis of the delay between two light curves at different energies and obtained the time delay as a function of the Fourier frequency, inversely proportional to the time. Their results show a break in the Fourier transform of the time delay, which occurs at the Fourier frequency corresponding to the time when low-energy photons start to arrive before the high-energy ones. Such a temporal evolution of the delay is a consequence of the mechanisms generating the X-ray flare considered in Lewis et al. (2016). Conversely, the LIV delay is expected to be constant along the flare as it is a cumulative effect over the propagation of all photons from the cosmic source to the Earth. It is entirely determined by the distance and the photon energies emitted by the source.

To find out the temporal evolution of the delays induced by the SSC model presented here, a simpler method is applied. The evolution of the delay is evaluated by comparing the time difference $\Delta t_{evol}(t)$ between two light curves F_1 and F_2 reaching the same normalized flux value and by computing this time difference all along the flare. **In other words, noting** the normalized fluxes of the two light curves F_1 and F_2 , and considering two times t and t_2 such as $F_1(t) = F_2(t_2)$, $\Delta t_{evol}(t) = t - t_2$. To compare this study with that of Lewis et al. (2016), we have to adopt their opposite sign convention for the time delays, meaning that in this section, a positive delay corresponds to low energies arriving after the high energies. The two light curves chosen for the comparison are integrated over the energy ranges 200 – 400 GeV and 2.6 – 4.7 TeV. The set of parameters considered here is the one presented in Table 1, corresponding to an acceleration-driven regime, but results can be obtained in the same way for the cooling-driven regime. The normalized light curves and the temporal evolution of the delay are shown in Figure 13. The result obtained here is similar to that shown in Figure 1 of Lewis

et al. (2016). At large times (small Fourier frequencies), the delay is large because the high-energy light curve decays faster than the low-energy one. A break occurs at the specific Fourier frequency corresponding to the time when a given flux is reached earlier for the high-energy light curve than for the low-energy one. At small times (large Fourier frequencies), the delay is negative because the high-energy flare rises after the low-energy one due to the time needed for electrons to be accelerated. Such results are in agreement with the analysis by Lewis et al. (2016) and confirm that intrinsic time delays can be significantly variable along the flares and show characteristic time profiles. This variation of the intrinsic time delays explains the result obtained in Section 4.1, concerning the CCF which cannot correctly reconstruct the injected delay. This is directly due to the fact that the CCF uses the full light curves to evaluate time delays.

To describe in the same way the situation when only a LIV time delay is present, two light curves were simulated, following the same asymmetric Gaussian shapes as the light curves coming from the SSC model. A constant time delay of $\Delta t = 500$ s is then injected between the two simulated light curves. The resulting temporal evolution of the delay is given in Figure 13, which illustrates the constant LIV time delay obtained as a function of the Fourier frequency. Such results clearly show that temporal evolution of time delays is a direct marker for the presence of intrinsic effects in flares observed from blazars.

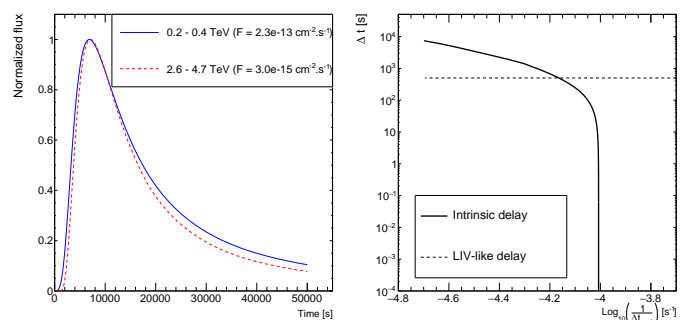


Fig. 13. Light curves for a flare with parameters of Table 1 with $B = 65$ mG for two energy bands (left) and evolution of the simulated time delays between them as a function of time (right). The LIV-like delay overlaid for comparison has been obtained by simulating two asymmetric Gaussian light curves with an injected constant delay of $\Delta t = 500$ s. Only positive delays are shown here in logarithmic scale, which can be directly compared to the Lewis et al. (2016) description.

7. Conclusion

The blazar flare model considered in this paper describes the evolution of a population of relativistic electrons radiating in a single compact zone through their synchrotron-self-Compton emission. In order to explore basic intrinsic energy-dependent time delays expected in such sources, we focus on a minimal scenario taking into account only the dominant processes needed to generate flares, namely a generic acceleration mechanism and radiative cooling in a slowly varying magnetic field. Under reasonable assumptions, an analytical solution can outline the electron spectrum evolution and applies for instance

when synchrotron losses dominate over inverse-Compton losses. Such a scenario clearly emphasizes the likely presence of significant intrinsic time delays. It reveals the existence of two main time-delay regimes, referred to here as acceleration-driven and cooling-driven regimes, over a large domain of parameters. The system evolves in one of these two regimes depending on the mechanism driving the evolution of the most energetic electrons at the time when the light curves reach their peak and the flare starts to decay. The cooling-driven regime typically corresponds to cases where the decay of the flare is mostly dominated by the radiative cooling effects. Conversely, the acceleration-driven regime corresponds to cases where the acceleration of emitting VHE electrons goes on while the flare starts to decay under the influence of some loss mechanisms other than radiative cooling, such as decrease of the ambient magnetic field or adiabatic losses. The confirmed detection of one of these regimes during blazar monitoring would provide precious information on detailed processes generating flares and significant measurements of time delays would further constrain source parameters *in situ*.

However, only upper limits on time delays have been firmly confirmed so far in TeV blazar flares. The detection of possible time delays in a flare of Mrk 501 has remained unique and was observed by only one instrument. Such a situation could be due to the lack of high-quality data on blazar flares. It could also directly put basic flare scenarios into question, which will require further investigation. In the most simple scenarios with fast initial injection or acceleration of particles immediately followed by flare decay due to radiative losses, a cooling-driven regime could have already been observed during bright flaring events since the cooling time over the VHE domain is longer than the time resolution reached. Radiative cooling alone should typically induce intrinsic time delays of several minutes. The fact that such lags have not yet been detected suggest that flares could mainly occur in a specific range of parameters, corresponding to an intermediate zone between the two time-delay regimes identified in this paper. As a consequence, there should be a physical link between acceleration and cooling processes with fine-tuning effects during the global evolution of the flare. A possible qualitative scenario would be to consider launching the flare by sudden shock acceleration or magnetic reconnection in the emitting zone, with subsequent mechanisms which induce the flare decay by adiabatic expansion and/or magnetic field decrease, while acceleration processes are still efficient enough at the highest energies. Future observations will be necessary to constrain scenarios and improve time-dependent modeling of blazar flares.

Moreover, the intrinsic delays obtained within the SSC scenario show specific characteristics which could help to constrain QG models or new physics involving time delays. The temporal dependency of the intrinsic delays appears to be different from the one expected by the current description adopted for LIV effects, which may provide a characteristic signature for the presence of intrinsic effects. Indeed, LIV delays are not expected to show any kind of evolution with time since they affect photons in the same way throughout their propagation. On the contrary, intrinsic delays evolve with time due to the different energy-dependent mechanisms involved in the generation of blazar flares. In addition, the energy dependency of intrinsic time delays at GeV-TeV energies was found to present typical power index

α in the range [0.45 – 0.85]. This property can be explored in order to test specific QG models which predict energy-dependent LIV delays with an index different from the typical intrinsic one. Nevertheless, further study of QG models involving LIV effects is necessary to fully exploit the global time-delay information when it becomes available and to distinguish between the various effects. Another important feature to exploit is that LIV delays depend strongly on the propagation distance while intrinsic delays should not.

Briefly, tools and results presented in this paper contribute to the scientific preparation of the new gamma-ray instruments of the coming decade which should provide higher sensitivity and a much larger number of blazar flare detections than current IACTs. Future data will potentially lead to the detection of significant time delays. Flare scenarios should be further developed in order to explain the new observables on intrinsic time delays, and to help disentangle intrinsic and extrinsic effects, opening a way for time-of-flight LIV searches.

References

- Abdalla, H., Aharonian, F., Ait Benkhali, F., et al. 2019, *ApJ*, 870, 93
- Abramowski, A., Acero, F., Aharonian, F., et al. 2012, *A&A*, 539, A149
- Abramowski, A., Aharonian, F., Ait Benkhali, F., et al. 2011, *Astroparticle Physics*, 34, 738
- Abramowski, A., Aharonian, F., Ait Benkhali, F., et al. 2015, *ApJ*, 802, 65
- Acharya, B. S., Agudo, I., Al Samarai, I., et al. 2019, *Science with the Cherenkov Telescope Array*, ed. World Scientific (338 pages)
- Aharonian, F., Akhperjanian, A. G., Barres de Almeida, U., et al. 2008, *Physical Review Letters*, 101, 170402
- Albert, J., Aliu, E., Anderhub, H., et al. 2007, *ApJ*, 669, 862, *astro-ph/0702008*
- Albert, J., Aliu, E., Anderhub, H., et al. 2008, *Physics Letters B*, 668, 253, *arXiv:0708.2889*
- Altschul, B. 2005, *Phys. Rev. D*, 72, 085003
- Altschul, B. 2006, *Phys. Rev. D*, 74, 083003
- Amelino-Camelia, G. 2013, *Living Reviews in Relativity*, 16, 5
- Amelino-Camelia, G., Ellis, J., Mavromatos, N. E., & Nanopoulos, D. V. 1997, *International Journal of Modern Physics A*, 12, 607
- Amelino-Camelia, G., Ellis, J., Mavromatos, N. E., Nanopoulos, D. V., & Sarkar, S. 1998, *Nature*, 393, 763
- Bednarek, W. & Wagner, R. M. 2008, *A&A*, 486, 679
- Billier, S. D., Breslin, A. C., Buckley, J., et al. 1999, *Physical Review Letters*, 83, 2108, *gr-qc/9810044*
- Biteau, J. & Williams, D. A. 2015, *ApJ*, 812, 60
- Blandford, R. D. & Königl, A. 1979, *ApJ*, 232, 34
- Böttcher, M., Mause, H., & Schlickeiser, R. 1997, *A&A*, 324, 395
- Bourgoin, A., Le Poncin-Lafitte, C., Hees, A., et al. 2017, *Phys. Rev. Lett.*, 119, 201102
- Celotti, A., Maraschi, L., & Treves, A. 1991, *ApJ*, 377, 403
- Dai, Z., Daigne, F., & Mészáros, P. 2017, *Space Sci. Rev.*, 212, 409
- Edelson, R. A. & Krolik, J. H. 1988, *ApJ*, 333, 646
- Ellis, J., Mavromatos, N. E., & Nanopoulos, D. V. 2000, *General Relativity and Gravitation*, 32, 127
- Franceschini, A., Rodighiero, G., & Vaccari, M. 2008, *A&A*, 487, 837
- Gao, H., Wu, X.-F., & Mészáros, P. 2015, *ApJ*, 810, 121
- Götz, D., Laurent, P., Antier, S., et al. 2014, *MNRAS*, 444, 2776
- Jacob, U. & Piran, T. 2008, *JCAP*, 1, 031, *arXiv:0712.2170*
- Joshi, M. & Böttcher, M. 2011, *ApJ*, 727, 21
- Katarzyński, K., Sol, H., & Kus, A. 2001, *A&A*, 367, 809
- Katarzyński, K., Sol, H., & Kus, A. 2003, *A&A*, 410, 101
- Kostelecký, V. A. & Mewes, M. 2008, *ApJ*, 689, L1, *arXiv:0809.2846*
- Kostelecký, V. A. & Mewes, M. 2009, *Phys. Rev. D*, 80, 015020, *arXiv:0905.0031*
- Kostelecký, V. A. & Russell, N. 2011, *Reviews of Modern Physics*, 83, 11
- Kostelecký, V. A. & Mewes, M. 2017, *Phys. Lett.*, B766, 137
- Le Poncin-Lafitte, C., Hees, A., & Lambert, S. 2016, *Phys. Rev.*, D94, 125030
- Lewis, T. R., Becker, P. A., & Finke, J. D. 2016, *ApJ*, 824, 108

- 957 Marscher, A. P. & Gear, W. K. 1985, *ApJ*, 298, 114
958 Mattingly, D. 2005, *Living Reviews in Relativity*, 8, cited on
959 19/04/2018, <http://www.livingreviews.org/lrr-2005-5>
960 Perennes, C., Sol, H., & Bolmont, J. 2017, *PoS, ICRC2017*, 611
961 Rosati, G., Amelino-Camelia, G., Marciandò, A., & Matassa, M. 2015,
962 *Phys. Rev. D*, 92, 124042
963 Sokolov, A., Marscher, A. P., & McHardy, I. M. 2004, *ApJ*, 613, 725
964 Tavecchio, F. & Bonnoli, G. 2016, *A&A*, 585, A25
965 Wei, J.-J. 2019, *MNRAS*, 485, 2401
966 Wei, J.-J., Wang, J.-S., Gao, H., & Wu, X.-F. 2016, *ApJ*, 818, L2
967 Zitzer, B. 2013, in *Proceedings, 33rd International Cosmic Ray Con-*
968 *ference (ICRC2013): Rio de Janeiro, Brazil, July 2-9, 2013*, 1147

969

970 Appendix A: Table for high-energy time delay

Parameter		$B_0 = 65$ mG		$B_0 = 90$ mG	
		ξ [s TeV $^{-\alpha}$]	α	ξ [s TeV $^{-\alpha}$]	α
m_b	1.0	175 ± 23	0.72 ± 0.1	-29 ± 8	0.57 ± 0.2
	1.25	300 ± 39	0.61 ± 0.1	154 ± 21	0.65 ± 0.1
	1.5	369 ± 59	0.49 ± 0.2	226 ± 29	0.63 ± 0.1
	2.0	391 ± 62	0.52 ± 0.2	365 ± 54	0.53 ± 0.2
δ	20	413 ± 90	0.68 ± 0.5	-97 ± 15	0.63 ± 0.3
	30	227 ± 32	0.59 ± 0.2	-46 ± 10	0.62 ± 0.3
	40	175 ± 23	0.72 ± 0.1	-29 ± 8	0.57 ± 0.2
	50	96 ± 14	0.47 ± 0.1	-26 ± 10	0.49 ± 0.3
A_0 [s $^{-1}$]	4.0×10^{-5}	264 ± 36	0.61 ± 0.2	69 ± 12	0.60 ± 0.2
	4.5×10^{-5}	175 ± 23	0.72 ± 0.1	-29 ± 8	0.57 ± 0.2
	5.0×10^{-5}	81 ± 14	0.50 ± 0.1	-125 ± 18	0.63 ± 0.1
	5.5×10^{-5}	-	-	-202 ± 28	0.57 ± 0.1
	6.0×10^{-5}	-72 ± 11	0.58 ± 0.1	-225 ± 27	0.80 ± 0.1
m_a	4.7	51 ± 9	0.62 ± 0.1	-205 ± 28	0.59 ± 0.1
	5.0	94 ± 13	0.65 ± 0.1	-106 ± 15	0.66 ± 0.1
	5.3	158 ± 24	0.48 ± 0.2	-75 ± 12	0.67 ± 0.2
	5.6	175 ± 23	0.72 ± 0.1	-29 ± 8	0.57 ± 0.2
	5.9	190 ± 26	0.61 ± 0.2	-	-
n	2.2	-	-	52 ± 11	0.43 ± 0.1
	2.3	173 ± 22	0.80 ± 0.1	-	-
	2.4	175 ± 23	0.72 ± 0.1	-29 ± 8	0.57 ± 0.2
	2.5	277 ± 153	0.26 ± 0.3	-72 ± 20	0.44 ± 0.2
	2.6	113 ± 26	0.66 ± 0.6	-104 ± 37	0.81 ± 0.7
	2.7	-	-	-	-
	2.8	-	-	-	-
$\gamma_{c,0}$	2×10^4	401 ± 51	0.64 ± 0.2	241 ± 31	0.66 ± 0.2
	3×10^4	265 ± 37	0.55 ± 0.2	57 ± 9	0.85 ± 0.2
	4×10^4	175 ± 23	0.72 ± 0.1	-29 ± 8	0.57 ± 0.2
	5×10^4	84 ± 13	0.57 ± 0.1	-82 ± 12	0.78 ± 0.2
	6×10^4	61 ± 14	0.42 ± 0.1	-131 ± 19	0.61 ± 0.1
	7×10^4	-	-	-151 ± 21	0.63 ± 0.1
	8×10^4	-	-	-205 ± 30	0.54 ± 0.1

Table A.1. Energy-dependent time-delay index for all investigated parameters for the two initial magnetic-field-strength values taken as benchmark values. Bold lines correspond to these benchmark cases, given by the parameters in Table 1. The missing values (shown with a dash) could not be evaluated because there was no significant delay in the considered energy range or because the maximum energy emitted was below 250 GeV.